sustainability

MDPI

Article

The Multiscale Assessment of Infrastructure Vulnerability to River Floods in Andean Areas: A Case Study of the Chibunga River in the Parish of San Luis, Ecuador

Daniel S. Paredes [1,*], E. Fabián Rivera [1,2], Paúl Baldeón-Egas [3] and Renato M. Toasa [3]

[1] Facultad de Ciencias de la Salud y del Ser Humano, Universidad Estatal de Bolívar, Guaranda 020101, Ecuador; edgar.rivera@ueb.edu.ec
[2] Facultad de Ciencias Agropecuarias, Recursos Naturales y del Ambiente, Universidad Estatal de Bolívar, Guaranda 020101, Ecuador
[3] Departamento de Ciencias de la Ingeniería, Universidad Tecnológica Israel, Quito 150522, Ecuador; pbaldeon@uisrael.edu.ec (P.B.-E.); rtoasa@uisrael.edu.ec (R.M.T.)
* Correspondence: daniel.paredes@ueb.edu.ec

Abstract

This research evaluates the vulnerability of public infrastructure in San Luis parish, Riobamba canton, Ecuador, to the flood risk posed by the Chibunga River under return period scenarios of 10, 50, 100, and 500 years. The main objective was to identify the most exposed systems—such as drinking water, sewerage, power grid, and utility poles—in order to prioritize mitigation measures. The methodology combined hydrometeorological analysis, hydraulic modeling using HEC-HMS and Iber, and the estimation of economic losses through the DaLA methodology. The results reveal that the low vulnerability of the drinking water system, as less than 0.08% of the network's length, is at risk in the high-to-very-high range, even in a scenario with a 500-year return period. On the other hand, there is evidence of high exposure of the sewerage network in extreme scenarios, considering that 49.15% is at high-to-very-high risk in the worst-case scenario. Furthermore, as the return period increases, there is a growing impact on the electrical network, where the proportion of assets at high-to-very-high risk increases from 0.60% to 6.88% for high voltage, 0.00% to 18.03% for low voltage, and 0.00% to 1.18% for streetlights for a return period of 10 to 500 years. It should be noted that the estimated direct economic losses amount to USD 84,162.86 when taking into account the worst-case scenario. In this regard, the novelty of this study lies in the integration of technical, hydraulic, and economic analyses for a scarcely studied rural Andean area, providing crucial data for preventive risk management. It concludes that investment in prevention is more cost-effective than post-disaster reconstruction, recommending the strengthening of the sewerage system's hydraulic capacity and the optimization of electrical infrastructure protection.

Keywords: infrastructure vulnerability assessment; territorial planning; Andean regions; floods; Ecuador

check for updates

Academic Editor: Hossein Bonakdari

Received: 9 July 2025
Revised: 17 August 2025
Accepted: 20 August 2025
Published: 3 September 2025

Citation: Paredes, D.S.; Rivera, E.F.; Baldeón-Egas, P.; Toasa, R.M. The Multiscale Assessment of Infrastructure Vulnerability to River Floods in Andean Areas: A Case Study of the Chibunga River in the Parish of San Luis, Ecuador. *Sustainability* **2025**, *17*, 7915. https://doi.org/10.3390/su17177915

Copyright: © 2025 by the authors. Licensee MDPI, Basel, Switzerland. This article is an open access article distributed under the terms and conditions of the Creative Commons Attribution (CC BY) license (https://creativecommons.org/licenses/by/4.0/).

1. Introduction

In recent years, climate change has intensified the frequency and magnitude of extreme hydrometeorological events, including river floods, that have resulted in both human and economic losses [1]. Consequently, this phenomenon poses a critical threat to communities settled in the Andean river basins, particularly in urban and rural contexts that lack

resilient infrastructure. Beyond their immediate effects, floods also compromise long-term sustainability, as they disrupt water security, agricultural productivity, energy supply, and transportation networks—the key dimensions of the United Nations Sustainable Development Goals (SDGs), particularly SDG 6, which addresses clean water and sanitation, SDG 11 and SDG 13, which focuses on sustainable cities and communities in order to significantly reduce the number of deaths caused by disasters, including those related to water, and the number of people affected by them, and to substantially reduce the direct economic losses caused by disasters in comparison to global gross domestic product, with a particular emphasis on protecting the poor and people in vulnerable situations [2].

These threats and their impacts are exacerbated in scenarios characterized by high climate variability, deficient land use planning, and limited institutional capacity for risk management [3]. In the high Andean regions of Latin America, such events are intensified by a combination of geomorphological, climatic, and anthropogenic factors, such as unregulated urban expansion, deforestation of riparian zones, and deterioration of hydraulic infrastructure [4,5]. Addressing these challenges through preventive hydrological studies is not only a matter of reducing immediate disaster risk but also a pathway toward strengthening resilience and promoting sustainable territorial development.

Ecuador, due to its diverse topography and variable rainfall regime, frequently experiences extreme events associated with torrential rainfall, which have increased in recent decades due to the El Niño phenomenon and global climate change [6]. These conditions have led to recurrent river overflows that cause severe impacts on the population, public infrastructure, and basic services. In this context, the Chibunga River—which flows through the San Luis parish in the Riobamba canton—has shown potentially dangerous fluvial behavior during heavy rainfall seasons. The area exhibits a growing pattern of vulnerability due to unplanned urban development, limited drainage capacity, and the exposure of critical infrastructure such as potable water systems, sewer networks, power lines, and communication routes. The lack of understanding of the river's hydraulic behavior and the associated risks under long return periods (10, 50, 100, and 500 years) has hindered the implementation of effective prevention and response policies. These vulnerabilities highlight the urgent need to design adaptation measures that guarantee long-term safety and resilience, ensuring that essential services and infrastructure can withstand extreme events, while promoting equitable and sustainable development.

1.1. Problem

The lack of comprehensive studies modeling the threat of flooding from the Chibunga River, together with the identification of critical areas of social and infrastructural exposure, represents a significant gap in hydrological risk management in the parish of San Luis. Although there are historical records of flooding, no multiscale hydrodynamic analysis has been developed to anticipate the effects of extreme events in different threat scenarios [7]. This compromises territorial planning, water security, and the operation of essential public service systems, especially in conditions of structural and climatic vulnerability.

1.2. Prism Focus

To provide a theoretical foundation for this research, a systematic literature review was conducted following the PRISMA methodology. The process included the identification, screening, and qualitative synthesis of peer-reviewed studies published between 2016 and 2024 in reputable scientific databases such as ScienceDirect, SpringerLink, MDPI, and IEEE Xplore. The keywords used in the search strategy were "flood risk", "hydraulic modeling", "flood hazard mapping", "river overflow", "Andean basins", and "climate change adaptation". From an initial set of 134 articles, a total of 23 studies met the inclusion criteria, which

required full-text access, application of hydraulic or hydrological modeling tools, and geographic relevance to mountainous or developing regions. Ultimately, nine studies were selected based on methodological rigor and direct applicability to the dynamics observed in the Chibunga River basin. The complete flowchart of the selection process is illustrated in Figure 1.

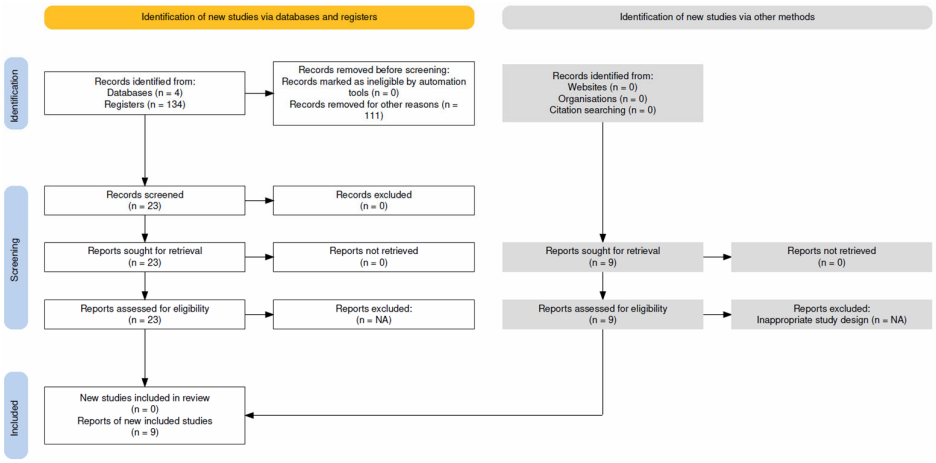


Figure 1. PRISMA 2020 flow diagram illustrating the identification, screening, and inclusion of studies in the systematic review.

The existing literature on flood vulnerability in mountainous regions consistently evidences an increasing risk driven by climate variability, insufficient land use planning, and the limited resilience of critical infrastructure [8,9]. In the context of Andean watersheds, Ref. [10] documents how extreme precipitation events, combined with anthropogenic pressures such as deforestation and unregulated urban expansion, exacerbate flood susceptibility. Research in Ref. [11] highlights that small urban settlements adjacent to riverbanks present high sensitivity to overflow events, particularly when early warning systems and drainage infrastructure are absent. From a technical standpoint, studies such as Ref. [12] validates the applicability of hydraulic modeling tools like HEC-RAS v6.6 (U.S. Army Corps of Engineers, Hydrologic Engineering Center, Davis, CA, USA) and Iber v2.4.5 (Flumen Research Institute—Universitat Politècnica de Catalunya & International Centre for Numerical Methods in Engineering, Barcelona, Spain; GEAMA—University of A Coruña, A Coruña, Spain), for simulating flood propagation and delineating hazard zones under various return periods, demonstrating their utility in vulnerability mapping. In high-altitude Latin American settings, Ref. [13] reports persistent modeling challenges, including steep slopes, fragmented hydrological networks, and the scarcity of high-resolution topographic data, which reduce predictive accuracy.

Collectively, these studies reinforce the need for localized, high-resolution assessments that integrate geomorphological constraints, infrastructure fragility, and socio-economic vulnerability—factors particularly relevant to rural Ecuadorian contexts [14]. This research addresses that gap by combining hydraulic simulations, exposure mapping, and risk quantification adapted to the geomorphology and data limitations of the Chibunga River basin. Unlike broader global analyses, the proposed approach integrates flood hazard modeling with infrastructure-specific vulnerability metrics and applies them within a multiscale framework. Furthermore, consistent with recommendations from Ref. [15], it aligns technical modeling outputs with participatory risk management, ensuring that simulation results can directly inform prevention and mitigation strategies in under-resourced Andean communities.

1.3. Gaps and Limitations in Literature

The PRISMA-based literature review identified three critical gaps that justify the approach adopted in this study. First, while hydraulic modeling and flood hazard mapping have been extensively applied in urban and rural contexts, most documented cases originate from regions with advanced monitoring networks, abundant hydrometeorological data, and well-developed infrastructure [9,12]. This contrasts sharply with rural Andean areas such as San Luis, Riobamba, where instrumentation is sparse, and continuous data records are lacking, limiting the transferability of conventional methodologies.

Second, the literature shows minimal integration of socio-territorial variables—such as the spatial distribution and exposure levels of critical infrastructure [16] (drinking water, sewerage, electricity, and road networks) and the demographic vulnerability of populations in hazard-prone zones. Although some studies have begun to incorporate social vulnerability indicators [14,15], their application in hydrological modeling for Latin America's mountainous regions remains limited. Most research focuses primarily on hydrodynamic behavior without linking hazard outputs to infrastructure impact assessments or territorial planning frameworks [8]. Lastly, there is a notable methodological gap concerning the calibration and validation of coupled hydrological–hydraulic models in high-slope basins with heterogeneous land uses and low data density. While existing tools [17] have proven to be technically effective in other settings, their adaptation to small high-Andean catchments has not been systematically documented, constraining their use for locally informed decision making.

In line with the above, this study addresses these limitations through an integrated approach that combines hydrological–hydraulic modeling with geospatial analysis of critical infrastructure and exposure levels, evaluated over different return periods of 10, 50, 100, and 500 years. It also incorporates a territorial vulnerability perspective that considers both the physical behavior of the event and its potential social and structural impacts. This approach fills a substantial gap in the literature, providing contextualized empirical evidence that can serve as a basis for mitigation and risk management strategies in similar territories.

2. Materials and Methods

2.1. Study Area

This study was carried out in the parish of San Luis, in the canton of Riobamba (Ecuador), with the objective of evaluating the flood threat caused by the Chibunga River and its possible impact on critical infrastructure. The Territorial Planning Plan of the canton of Riobamba [18] mentions that the parish of San Luis is located within the central Sierra region of Ecuador, specifically in the province of Chimborazo, which is part of the canton of Riobamba and has an area of 2986.19 ha as illustrated in Figure 2. It is located approximately 5 km southeast of the urban center of Riobamba, at an elevation that ranges between 2584 and 2839 m above sea level. It should be noted that the United Nations Office for Disaster Risk Reduction [19] states that generating flood maps is a fundamental tool to understand the effects of climate change, because floods can cause significant economic losses, displacement of populations, and interruption of essential elements.

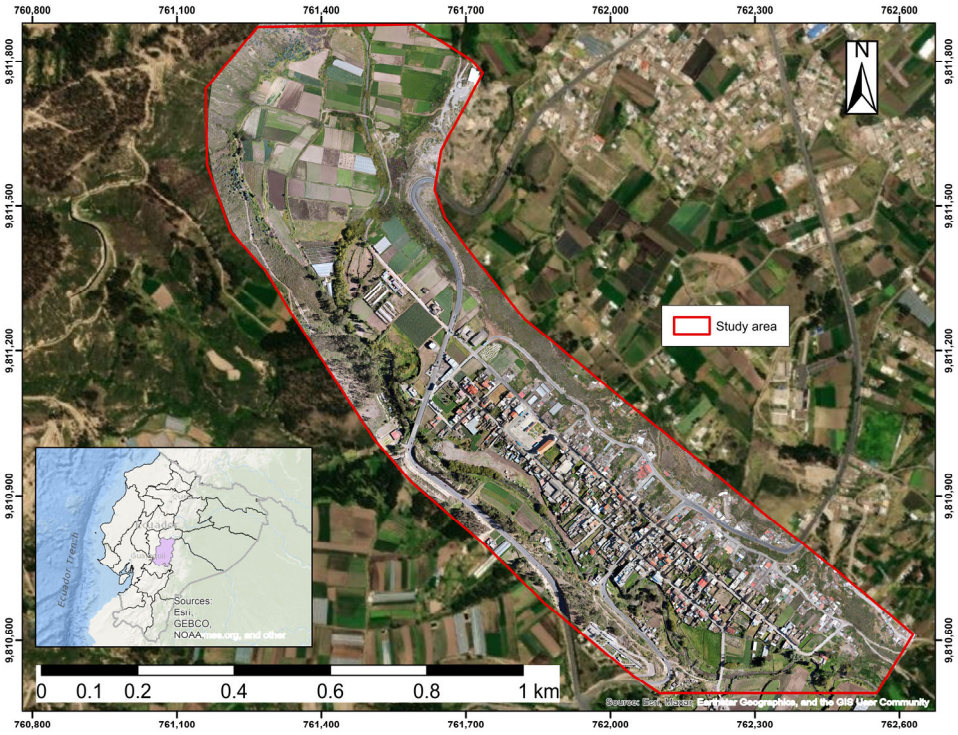


Figure 2. Site selected for flood hazard analysis (San Luis parish, Riobamba canton).

2.2. Overview of the Methodology

The methodology of this project consists of two main phases: the first phase corresponds to data collection, and the second phase involves data processing using software associated with geographic information systems, in order to conduct a comprehensive flood hazard analysis.

The methodological workflow is innovative for the study region, located in an Andean area of Ecuador, and highlights the following sections: (i) It implements a multiscale temporal design that links basin-scale hydrologic modeling system HEC-HMS v4.12 (U.S. Army Corps of Engineers, Hydrologic Engineering Center, Davis, CA, USA) with 2D hydraulics at the reach/asset scale. (ii) It adopts a dual cost–benefit digital elevation model (DEM) architecture using an open-access, 12 m DEM obtained by the Advanced Land Observing Satellite (ALOS), which has a Phased Array L-band Synthetic Aperture Radar (PALSAR) imaging microwave radar. This DEM supports watershed-scale analyses, such as hydrographic network delineation, due to its low cost and sufficiency for first-order morphometric and hydrological tasks. On the other hand, the photogrammetric DEM, obtained using an unmanned aerial vehicle (UAV), DJI Air 2S (DJI, Shenzhen, China) with a resolution of 0.17 m, was used in Iber for 2D hydraulics at the section/active scale (microtopography, plain roughness, and flow paths). In effect, the high resolution improves the representation of depth and velocity, as well as the extent of the flood, with lower cost and survey time than Light Detection and Ranging (LiDAR), which strengthens the validity of local mapping and the reliability of the model [20,21]. (iii) It relates 2D depth and velocity simulations to an adapted Damage and Loss Assessment (DaLA) loss model. (iv) It applies a calibration and validation protocol.

Figure 3 provides a schematic representation of the methodology used in this research.

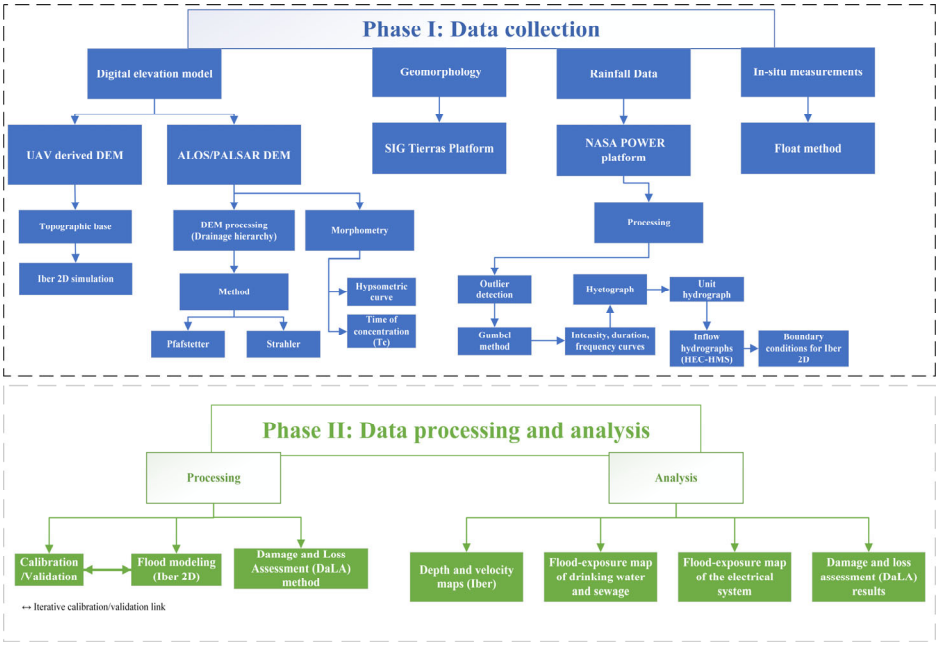


Figure 3. Flowchart of the methodology for flood susceptibility mapping.

2.3. Phase I: Data Collection

In phase 1, which corresponds to data collection, geospatial data were acquired, such as the DEM downloaded from the Alaska Satellite Facility platform, which obtains data from the Japanese ALOS satellite with its PALSAR sensor, which according to Earth Data [22] is an effective tool for the analysis of topography where we can find spatial resolutions ranging from 10 to 30 m, depending on the processing level and product type. In this sense, for the present work, the ALOS PALSAR Radiometrically Terrain-Corrected (RTC) product, v3.0 (Alaska Satellite Facility—ASF DAAC, University of Alaska Fairbanks, Fairbanks, AK, USA; data from Japan Aerospace Exploration Agency—JAXA, Tokyo, Japan) was used, based on imagery acquired between 2006 and 2011, and processed to a 12 m pixel resolution, which is an input for the analysis of the hydrographic network of the study area.

This DEM was processed using ArcGIS 10.8 (Esri, Redlands, CA, USA), which includes hierarchical drainage network classification tools such as Pfafstetter and Strahler. It is important to note that the Pfafstetter method allows for the hierarchical classification of watersheds by identifying the main watershed and subdividing it into four sub-watersheds based on geomorphological characteristics and flow direction. Its application in flood studies is relevant as it allows for the definition of priority drainage areas. Furthermore, the Strahler method allows for the classification of drainage networks based on hydrological trees, where each node represents each river reach and the links represent river connections, helping to identify areas prone to high flow concentrations. An important component in flood analysis is the hypsometric curve that allows to identify if the basin is young (erosive), mature (in equilibrium), or senile (sedimentary), and this process is carried out from the processing of the DTM with hydrological geoprocessing tools present in the ArcGIS software, where elevation values (h) were extracted from the basin, and the next step is to calculate the accumulated relative area (A_T) (Equation (1)).

$$A_T = \frac{A_i}{A_{total}} \tag{1}$$

where (A_i) is the area above the elevation, and (A_{total}) is the total area of the basin.

In turn, the relative altitude is calculated, which allows for a normalized comparison of the distribution of elevations in a hydrographic basin. This facilitates the comparison

between different basins in order to know the degree of geomorphological evolution. This parameter is obtained by normalizing each altitude (h_i) with respect to the maximum altitude (h_{max}) (Equation (2)).

$$H_r = \frac{h_i - h_{min}}{h_{max} - h_{min}} \tag{2}$$

where (H_r) is the relative altitude (normalized value between 0 and 1), (h_i) is the altitude of a point or height interval within the basin, (h_{max}) is the maximum altitude within the basin, and (h_{min}) is the minimum altitude within the basin. After obtaining the values, the graphic representation is made, where if it is type A (convex), it is a young basin with strong erosion, if it is type B (sigmoid), it is a basin in equilibrium or a mature basin, and if it is type C (concave), it is an old basin with high sediment deposition.

Lithology, land use types, and geomorphology data were collected from SIGTIERRAS Geoportal—Sistema Nacional de Información y Gestión de Tierras Rurales e Infraestructura Tecnológica (Ministerio de Agricultura y Ganadería—MAG, Quito, Ecuador). These parameters are vital to evaluate their influence on flood dynamics, determining the permeability of the terrain, the modification of runoff patterns, and the identification of areas prone to water accumulation and river overflows.

It is important in flood analysis to know the behavior of hydrological and meteorological data in the study area, which is why historical rainfall data from 2001 to 2023 from NASA's Prediction of Worldwide Energy Resources (POWER), Service v2.4.5, Data v10.1.1 (NASA Langley Research Center, Hampton, VA, USA). platform were used, which provided relevant information on spatial and temporal patterns, essential for hydrological modeling. The use of this dataset is justified due to the limited availability of local meteorological stations with continuous historical records. In addition to the above, for the processing of these data, statistical processing of outliers was carried out based on logarithmic transformations and statistical criteria (thresholds) in order to detect doubtful data. Precipitation data usually present a skewed distribution. The application of the logarithmic transformation serves to stabilize the variance, which facilitates the identification of extreme values (Equation (3)).

$$log\ log\ (P_{24\ hr}) = Y \tag{3}$$

where (Y) represents precipitation values on a logarithmic scale, and (P) represents the accumulated rainfall over 24 h. Similarly, outliers can be identified, which allows for the identification of unusual weather events, measurement errors, or data biases. Therefore, the outlier method, based on statistical thresholds (Equation (4)), was used.

$$\begin{aligned} x_H &= \overline{x} + k_n \times s \\ x_L &= \overline{x} - k_n \times s \end{aligned} \tag{4}$$

where $\overline{x}$ is a media, (k_n) is a coefficient dependent on the sample size (n), x_H is the upper threshold for doubtful values, and (x_L) is the lower threshold for doubtful values. These values correspond to the acceptance thresholds expressed on a logarithmic scale. To reverse the logarithmic transformation and recover the maximum and minimum admissible precipitation values on their original scale, the exponential function (antilogarithm) is applied (Equation (5)).

$$\begin{aligned} P_H &= 10^{xH} \\ P_L &= 10^{xL} \end{aligned} \tag{5}$$

where (P_H) is the maximum accepted precipitation, and (P_L) is the minimum accepted precipitation. The Gumbel method is a probabilistic model for estimating extreme precipitation events, allowing the maximum expected precipitation to be estimated for different

return periods. This method was carried out using the following calculations. First, the mean ($\overline{x}$) of the precipitation was determined, which represents the average value of the data series (Equation (6)).

$$\overline{x} = \frac{\sum x_t}{n} \tag{6}$$

where ($\overline{x}$) is the mean precipitation in mm, (x_t) is the precipitation value at time (t) in mm, and (n) is the total number of data values. The standard deviation (S) was then calculated to assess the dispersion of the values with respect to the mean (Equation (7)).

$$S = \sqrt{\frac{\sum_{i=1}^{n} (x_t - \overline{x})^2}{n-1}} \tag{7}$$

where (S) is the standard deviation in mm, ($\overline{x}$) is the average precipitation in mm, (x_t) is the precipitation value over time (t) in mm, and (n) is the total number of data values. From these parameters, we obtain the scale parameter (α), which measures the variability of extreme events (Equation (8)).

$$\alpha = \frac{\sqrt{6}}{\pi} \times S \tag{8}$$

where (α) is the scale parameter, (S) is the standard deviation in mm, and (π) is the mathematical constant. The location parameter (u) is then defined, which defines the threshold over which the precipitation values are distributed (Equation (9)).

$$u = \overline{x} - 0.5772 \times \alpha \tag{9}$$

where (u) is the location parameter in mm, ($\overline{x}$) is the average precipitation in mm, (α) is the scale parameter in mm, and 0.5772 is the Euler–Mascheroni constant. Subsequently, the reduced variable (Y_t) was obtained (Equation (10)).

$$Y_t = -ln\ ln\left(ln\ ln\left(\frac{T}{T-1}\right)\right) \tag{10}$$

where (Y_t) is the dimensionless reduced variable, (T) is the return period in years, and (ln) is the natural logarithm. It allows to calculate the maximum expected precipitation (X_t) based on the return period (Equation (11)).

$$X_t = u + (\alpha \times Y_t) \tag{11}$$

where (X_t) is the maximum estimated precipitation in mm, (u) is the location parameter in mm, (α) is the scale parameter in mm, and (Y_t) is the dimensionless reduced variable.

The calculation of intensity, duration, and frequency (IDF) curves allows estimating the expected precipitation intensity for different return periods (10, 50, 100, and 500 years) and in turn to have information on how stormwater will disperse and which areas will be prone to flooding (Equation (12)).

$$I = \frac{K \times T^m}{D^n} \tag{12}$$

where (I) is the precipitation intensity expressed in mm/h, (T) is the return period, which represents the frequency of a rainfall event of a certain intensity, (D) is the duration of rainfall measured in hours or minutes, and (K), (m), and (n) are regression coefficients estimated by log-linear regression, $\ln I = lnK + mlnT - nlnD$, using least squares over all (T, D) pairs.

The time of concentration is calculated using the California formula, which allows estimating the time required for water to flow from the most distant point in the basin to

its outlet, allowing for a precise characterization of the hydrological behavior of the system (Equation (13)).

$$T_c = 0.066 \times \left(\frac{L}{J^{0.55}}\right)^{0.77} \quad (13)$$

where (L) is the main channel length, and (J) is the slope.

Based on the same return periods, hyetographs (the relationship between the intensity and duration of a precipitation event) are developed to observe the distribution of precipitation over time. With this information, the unit hydrograph was generated using the HEC-HMS software, incorporating both direct runoff and baseflow components, which describes the variation in flow in a basin in response to a single precipitation event uniformly distributed over the drainage surface. This study uses a multiscale, temporal approach to model the hydrological and hydraulic responses for multiple return periods (10, 50, 100, and 500 years), representing increasingly extreme flood scenarios. For each return period, design and inflow hydrographs were developed and simulated independently in Iber. This enables us to evaluate progressive changes in flood dynamics, exposure, and infrastructure vulnerability across a range of plausible temporal extremes. On the other hand, the time of concentration in the basin was calculated using the California Highway method to determine the time required for an intense storm to generate maximum flow in the river. On the other hand, field measurements of the river discharge were made using the float method in three cross-sections of the Chibunga River, allowing the flow to be estimated in natural and artificial bodies of water. It is based on the measurement of the surface velocity of the water from the time it takes a floating object to travel a known distance. According to Cerdan and Valdivia [23], in their study, they evaluated the accuracy of the float method in rectangular section channels, finding that its accuracy exceeded 75%.

2.4. Phase II: Data Processing and Analysis

In phase 2, processing and analysis were carried out. Prior to performing the flood simulation, the DEM must be cleaned, removing unwanted elements such as bridges, bushes, and other elements present on the river banks. Subsequently, modeling is carried out using the Iber software, generating a two-dimensional hydraulic model that simulates water flow in rivers and floodplains, providing maps of the extent, depth, and speed of flooding in the study area. Ref. [20] states that Iber is an open-source and freely accessible software application, characterized by a visually attractive but not entirely intuitive user interface, and in turn provides georeferenced two-dimensional spatial outputs that are advantageous for facilitating communication and performing risk assessments. The main equations governing this type of simulation are the Saint-Venant equations, which represent the behavior of moving water in a two-dimensional domain. In this sense, the Saint-Venant equation for mass conservation is defined as follows:

$$\frac{\partial h}{\partial t} + \nabla \times (h \times u \rightarrow) = 0 \quad (14)$$

where (h) is the depth of water at a given point in meters, ($u \rightarrow$) is the flow velocity vector, (t) is time, and ∇ represents the divergence operator (mathematical expression of the variation in the flow in a coordinate system).

Regarding the conservation of momentum equation, we have the following:

$$\frac{\partial (h \times u \rightarrow)}{\partial t} + \nabla \times (h \times u \rightarrow \otimes u \rightarrow + \tau) = -gh\nabla\eta \quad (15)$$

where (τ) is the tension sensor (representing the friction and resistance in the flow), (g) is acceleration due to gravity, and (η) is the elevation of the land. It should be noted that these

equations are solved numerically in Iber using finite difference or finite volume methods. This software applies a temporal and spatial discretization scheme in a grid of cells, where the two-dimensional flow simulation is performed.

In addition, using the ArcGIS software, the flood maps generated in Iber were overlaid with data on critical infrastructure, such as water supply systems, sewage networks, and electrical grids provided by the Risk Management Unit of the Gobierno Autónomo Descentralizado of Riobamba canton, to assess their vulnerability to the threat of flooding at different return times.

Finally, it is important in disaster risk management to estimate the economic losses derived from a hydrometeorological hazard such as a flood. In this regard, an adapted version of the DaLA method was applied, which is a tool developed by the Economic Commission for Latin America and the Caribbean (CELAC) that provides a methodological structure for quantifying damages and losses. It should be noted that the approach consists of three key stages: (1) identification of the affected infrastructure, (2) estimation of the degree of damage, and (3) calculation of economic damage by multiplying the amount affected by a unit replacement value at current prices. It should be noted that unit costs were obtained from unit price analyses (UPAs) of local and national public utilities. For water and sanitation, the resolutions of the Empresa Municipal de Agua Potable y Alcantarillado of the city of Riobamba (EMAPAR) and the bidding annexes, which specifically include the UPAs and reference budgets, were used. Regarding the electricity sector, for low and high voltage and poles, the UPAs and official price lists of the Corporación Nacional de Electricidad (CNEL EP) were used for distribution works. It should be noted that the Sistema Oficial de Contratación Pública de Ecuador was the primary source of information [24]. Therefore, damage to critical infrastructure was estimated for the worst 500-year flood scenario, where the amount affected is defined as follows:

$$Amount\ involved = total\ amount \times \left(\frac{percentage\ of\ damage}{100}\right) \tag{16}$$

where amount involved is the length in meters or number of units affected, and percentage of damage is the percentage of infrastructure in high and very high hazard zones.

The direct economic damage is then calculated as follows:

$$Estimated\ damage\ (USD) = amount\ involved \times unit\ cost\ (USD) \tag{17}$$

where the (*unit cost*) is the value per meter or per unit, and includes materials, excavation, installation, replacement, and labor.

The total sum of damages was calculated with the following formula:

$$Total\ damage = \sum_{i=1}^{n} (amount\ involved \times unit\ cost) \tag{18}$$

where the quantity affected and the unit cost of an operation are taken into consideration for all affected infrastructures.

3. Results

This section focuses on assessing the impacts caused by the flooding of the Chibunga River using the methodology explained above to determine the maximum precipitation in 24 h, as well as generating the corresponding hyetograph. The HEC-HMS software was used to create the hydrograph, which allowed for an accurate representation of the variation in flow over time. With the processed data, Iber, a software specialized in hydraulic modeling, was used to perform simulations that identified vulnerable elements

in different return periods: 10, 50, 100, and 500 years. These simulations provided an estimate of the potential impact of the river's flooding, which facilitated risk assessment and decision making in flood management.

The Chibunga River's flow was accurately estimated using the flotation method, an indirect technique that measures surface water velocity based on the time it takes a floating object to travel a given distance. A correction coefficient was applied to adjust for the difference between surface velocity and the mean flow rate. To improve accuracy and capture local variations, measurements were taken in three cross-sections of the river, ensuring a detailed representation of its hydrological conditions, as illustrated in Figure 4.

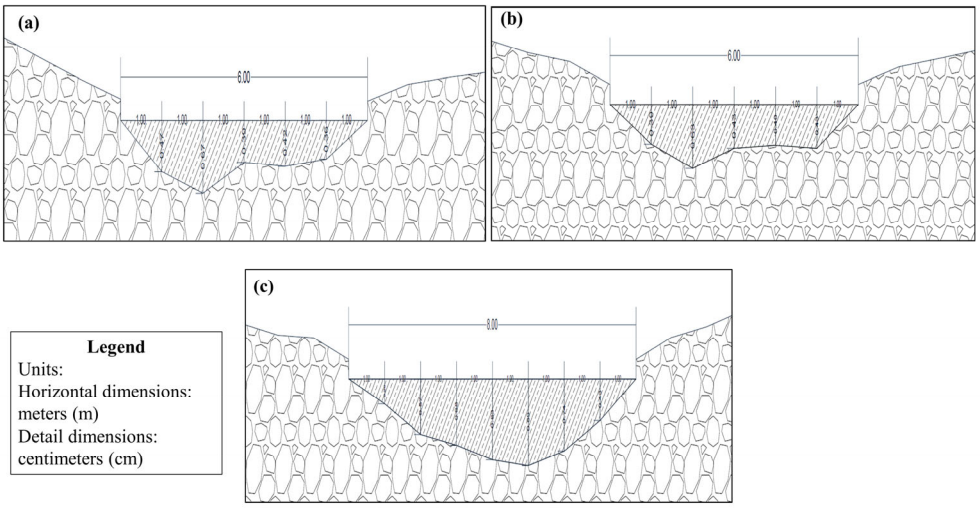


Figure 4. Cross-sectional profiles of the Chibunga River in the study area: (**a**) upstream reach; (**b**) middle reach; and (**c**) downstream reach.

In the three sections analyzed, the Chibunga River basin had a constant width of 6 m, with variations in depth and flow. In the first section, the maximum depth was 67 cm and the minimum depth was 36 cm, with a flow of 4 m^3/s. In the second section, the depth ranged between 63 cm and 36 cm, obtaining a flow of 3.35 m^3/s. In the third section, the depth varied between 89 cm and 26 cm, recording the highest flow of 4.09 m^3/s. Measurements were made using the flotation method, allowing for an assessment of flow dynamics in different sections of the river.

3.1. Determination of Doubtful Data

Outliers in the precipitation data were identified and analyzed to improve the accuracy of climate prediction. The logarithmic transformation and statistical thresholds presented in Equations (3) and (4) were used to detect potential anomalies in the maximum and minimum values recorded over a 24 h period each year. Previous studies highlight the importance of this technique in avoiding bias and improving the accuracy of risk assessment and decision making based on climate data.

The analysis of doubtful data established a threshold of 1.61 on the logarithmic scale for high values, with a maximum accepted rainfall of 40.98 mm, while the maximum observed value was 34.61 mm, indicating the absence of high doubtful data. For low values, the threshold was 1.23, with a minimum accepted rainfall of 16.83 mm, and the minimum recorded value was 17.00 mm, which also ruled out low doubtful data. To ensure data quality, the outlier methodology was applied to detect and correct outliers that could distort the analysis. These extreme values can originate from measurement errors, instrument failures, or unusual climate variations. The methodology made it possible to adjust or

eliminate extreme data, improving the accuracy of the analyses and strengthening the reliability of risk studies and decisions based on climate data.

Figure 5 shows that, between 2001 and 2023, rainfall variability peaked in 2018 and 2023, while levels were notably low in 2001, 2015, and 2019. These fluctuations reflect the influence of natural climatic factors in the region. Years with high rainfall increased the risk of flooding by exceeding the river's drainage capacity, while in drier years, the flow remained manageable, without ruling out the possibility of future overflows.

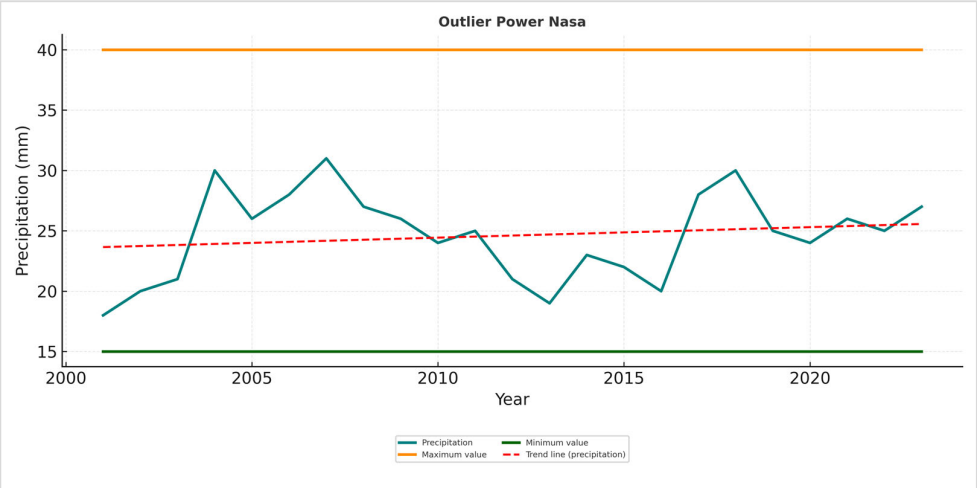


Figure 5. Annual precipitation from NASA POWER (2001–2023): QC thresholds and trend.

3.2. Extreme Precipitation and IDF Curves

Maximum precipitation was calculated using the Gumbel method, corresponding to different return periods, specifically 10, 50, 100, and 500 years. This method is widely recognized in hydrological studies for its ability to model extreme precipitation events. The Table 1 shows the calculation of maximum precipitation in 24 h.

Table 1. Gumbel (EV-I) estimates of 24 h precipitation quantiles for selected return periods.

Return Period T (Years)	Reduced Variate Y_t	Precipitation (mm) X_t (mm)	Probability of Occurrence F(xT)	Fixed-Interval Correction X_t (mm)
10	2.250	38.6	0.900	43.6
50	3.902	60.8	0.980	68.7
100	4.600	70.3	0.990	79.4
500	6.214	92.0	0.998	104.0

The analysis of maximum precipitation using the Gumbel method showed relevant results for different return periods: 43,591 mm for 10 years, 68,749 mm for 50 years, 79,385 mm for 100 years, and 103,962 mm for 500 years, with probabilities of occurrence of 0.9%, 0.98%, 0.99%, and 0.998%, respectively. These results are consistent with those of recent studies, such as Ref. [25] which reported similar values for the analyzed periods, validating the use of the Gumbel method in hydrological modeling. Likewise, the work of Ref. [26] supports these findings by documenting maximum precipitation consistent with the estimates obtained in this analysis.

The IDF curves were calculated using precipitation data provided by Power NASA, with the aim of estimating precipitation intensities for different return periods (10, 50, 100, and 500 years). This analysis was based on the formula used for calculating maximum intensities, which was supported by the work of Ref. [27] which offers a solid

theoretical framework for hydrological analysis and extreme precipitation estimation. The expected maximum intensity values in 1 h for each return period were calculated using Equation (12), whose results are as follows: 50.90 mm/h for 10 years, 68.75 mm/h for 50 years, 108.34 mm/h for 100 years, and 186.68 mm/h for 500 years.

The IDF curves in Figure 6 show that the heaviest rainfall occurs over short periods of time and more frequently affects less common events, such as the 500-year return period (T500). This behavior is crucial for the Chibunga River, since intense rainfall in a short period of time increases river flow, reducing infiltration and promoting rapid accumulation of water in the channel. This increases the risk of flooding in vulnerable areas, such as the San Luis parish in the Riobamba canton, especially during exceptional or intense rainfall events. To calculate the time of concentration for the Chibunga River basin, the California formula is used, a method widely used in hydrology. This formula estimates the time it takes for water to travel from the furthest point in the basin to the outlet, considering factors such as channel length and the basin's maximum gradient, and Tc = 207 min.

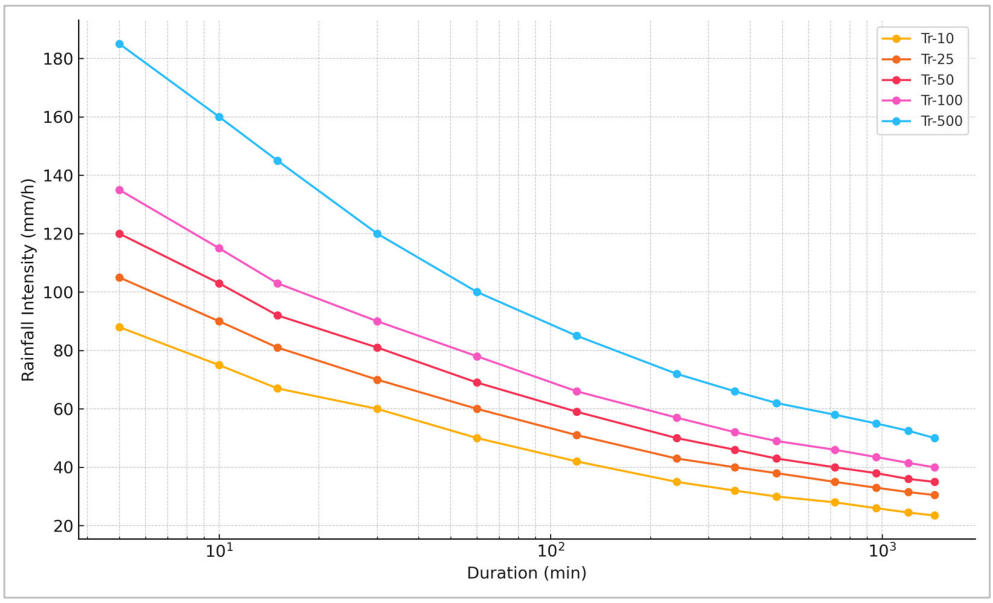


Figure 6. Intensity–duration–frequency (IDF) curves for return periods of 10, 25, 50, 100 and 500 years.

3.3. Hyetograph and Hydrograph Analyses for Return Periods of 10, 50, 100, and 500 Years

As shown in Figure 7, hyetographs describe the relationship between intensity (mm/h) and duration (min). They help us estimate the expected precipitation amount for a given location and time period, based on historical data. This allows us to estimate the expected precipitation amount in San Luis for different return periods: 10, 50, 100, and 500 years.

Time of concentration (Tc) is a key hydrological parameter that governs how a basin responds to intense rainfall events. Ref. [28] states that an error in the calculation of Tc can lead to an inaccurate estimate of the design flow. In the present study, however, a relatively short Tc of 138 min was obtained for the Chibunga River basin. This means that the flow generated in the most distant sectors quickly reaches the outlet, resulting in hydrographs with higher peaks and steeper rise curves. As the return period increases, the maximum intensity of the hydrographs grows, generating progressively higher peak flows. Higher flows translate into greater depths and velocities, widening the flood footprint and increasing the threat to essential elements such as sanitation infrastructure, drinking water supplies, and electricity networks, as demonstrated by comparable hydraulic simulations in Iber.

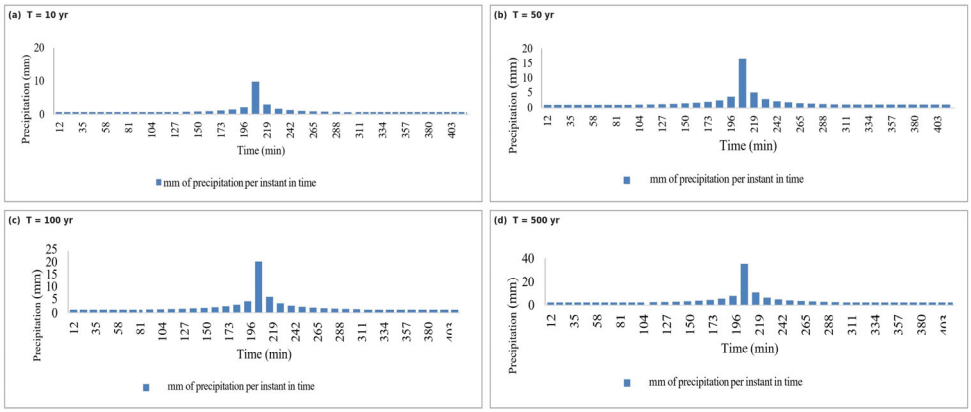


Figure 7. Design hyetographs (precipitation intensity–time; model input) used in the hydrological simulations for return periods: T = 10 (**a**), 50 (**b**), 100 (**c**), and 500 (**d**) years.

Analysis of the hyetographs shows that the maximum precipitation intensity increases with the return period. In all cases, the peak is recorded at minute 207, with values of 9.76 mm for 10 years, 16.54 mm for 50 years, 20.76 mm for 100 years, and 35.20 mm for 500 years. This shows that. the longer the return period, the more intense the extreme precipitation events.

A hydrograph is a graphical representation of a body of water's flow over time and is essential in hydrologic studies. Ref. [29] developed a method based on research in the Appalachian Mountains, establishing synthetic relationships for unit hydrographs in basins ranging from 30 to 30,000 km^2. Applying this method to the Chibunga River basin, with an area of 418 km^2, synthetic unit hydrographs can be obtained for return periods of 10, 50, 100, and 500 years.

As shown in Figure 8, the hydrographs shows how the Chibunga River's flow varies over different return periods. For a 10-year period, the initial flow was 0.2 m^3/s, reaching its maximum peak of 104.6 m^3/s at 210 min (3:50 h), and decreasing to 0.1 m^3/s at 738 min (12:30 h). For the 50-year period, the maximum flow increased to 422.3 m^3/s in the same time of 210 min, decreasing to 0.2 m^3/s in 744 min (12:40 h). For the 100-year period, the initial flow was 0.1 m^3/s, reaching a maximum of 681.7 m^3/s at 246 min (4:10 h) and decreasing to 0.2 m^3/s at 788 min (13:10 h). Finally, over a 500-year period, the peak flow reached 1728.9 m^3/s in 246 min, decreasing to 0.5 m^3/s in 788 min. These values indicate that, as the return period increases, the peak flow increases considerably, reflecting the intensification of surface runoff events.

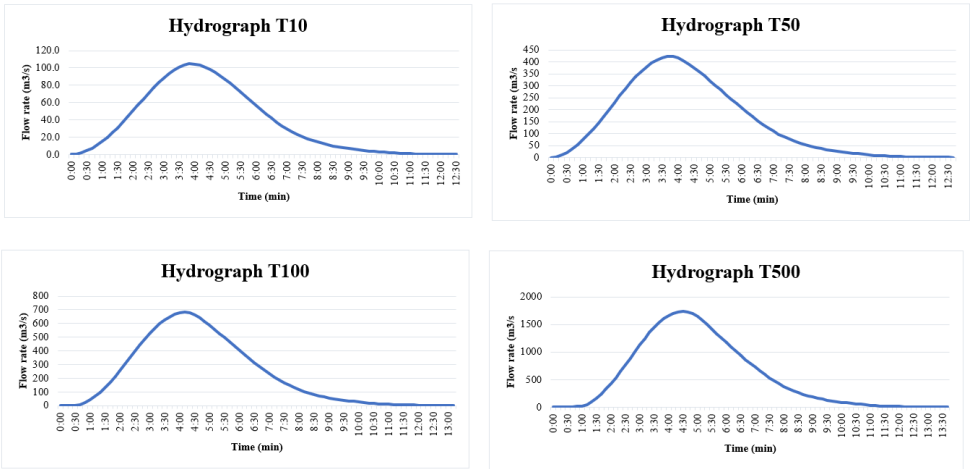


Figure 8. Hydrographs (discharge–time; model output) generated by HEC-HMS from Figure 7 hyetographs; inputs to the Iber hydraulic simulations.

3.4. Hydraulic Modeling of the Chibunga River Return Flows at 10, 50, 100, and 500 Years

3.4.1. Construction of the DEM

For hydraulic modeling, variables such as the digital elevation model, obtained by drone flight with a pixel resolution of 0.17 m × 0.17 m, are essential. As shown in Figure 9, the DEM is vital because it allows us to obtain the main channel of the basin and the morphology of the sector for constructing the Manning roughness.

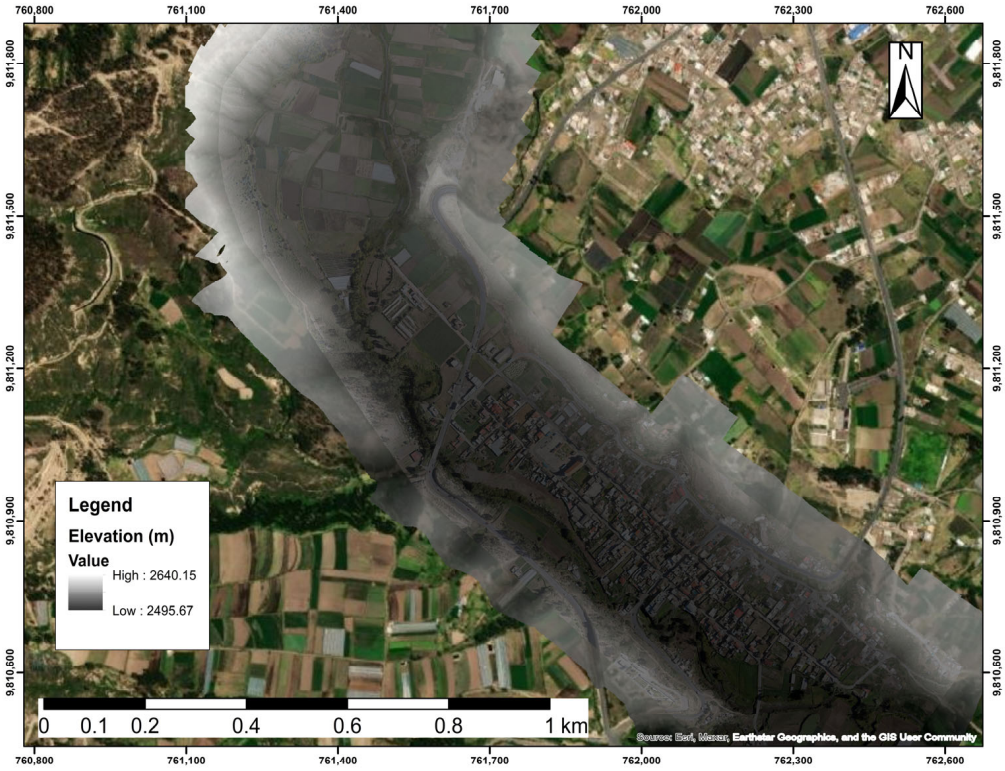


Figure 9. DEM model of the study basin.

3.4.2. Manning's Roughness

This variable is necessary to be able to determine, based on the use and cover of the land, how the water flow will behave, that is, if there will be more water volume or not depending on the type of vegetation cover; based on this, it is determined whether the water infiltrates or runs off the study area, and if there is more dense vegetation, then the water will behave differently below the values of Manning roughness for the hydraulic calculation. These values were assigned within the Iber software environment by spatially parameterizing the model according to land cover type, bed morphology, and vegetation density, integrating information obtained from field work and geospatial analysis. Figure 10 illustrates the assignment of Manning's roughness values and the classification of land-use categories employed in the model. Additionally, Manning's n values were taken from standard references [30–32], and mapped to land use and land cover categories and to municipal cadastral classes provided by the Riobamba municipal government.

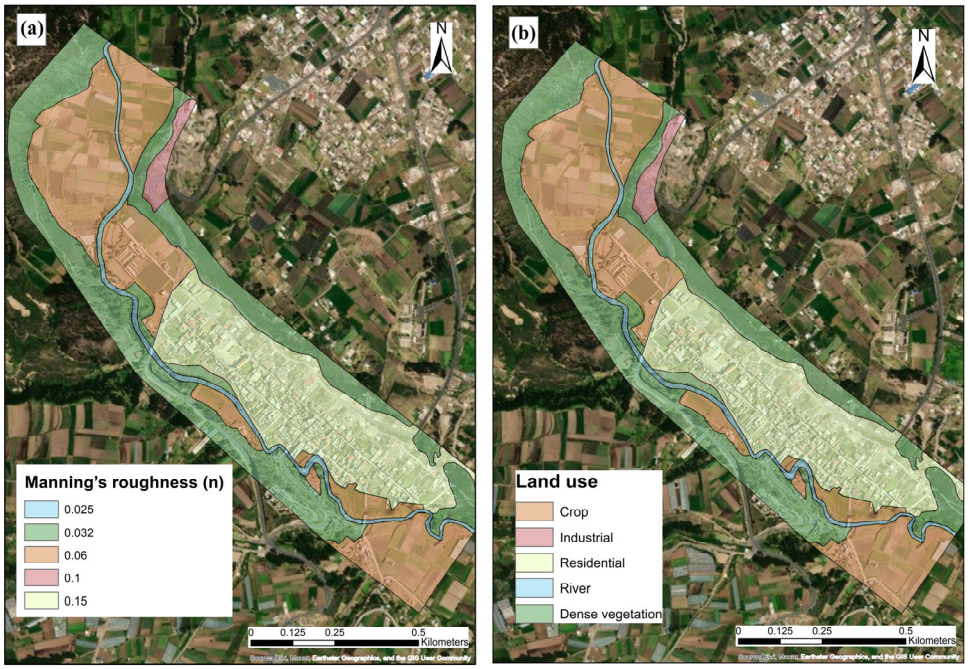


Figure 10. (**a**) Assigned Manning's roughness (n) per land use category and (**b**) land use classes.

3.4.3. Model Calibration and Validation

The Iber 2D configuration was calibrated by refining Manning's n according to land use and land cover classes (derived from municipal cadastral data and a field survey) within published ranges, until the simulated water surface profiles, sectional depths, and velocities were consistent with the observations. The numerical set-up solves the two-dimensional shallow-water (Saint-Venant) equations (Iber v2.4.5), with a variable time step, subject to stability constraints. Upstream inflows used the HEC-HMS design hydrographs for return periods (T = 10, 50, 100, and 500 years), while the downstream boundary condition is specified according to the local slope using the normal-depth/rating approach. The Manning roughness coefficient was assigned to land use and land cover classes according to published ranges. The adopted value for each class is reported for traceability purposes.

Validation was based on independent evidence at three levels: (i) comparison of the simulated levels and depths with in situ high-water marks and limnometric notes, with high-water marks deemed matched when modeled water-surface elevations were within $\pm$0.20 m of observations; (ii) qualitative contrast of sectional discharges and velocities with in situ estimates from the float method and hydrograph peaks; and (iii) overlaying the simulated flood extent with municipal and satellite mapping of preceding events. For flood-extent checks, we binarized simulated depth rasters at a threshold of 0.15 m to define operational inundation; results were qualitatively robust to thresholds in the range of 0.10–0.20 m. Overlays were interpreted in terms of true positives, false negatives, and false positives. Float method velocities were used as range checks given their known positive bias.

Under this temporal multiscale set-up, we compare depth, extent, and exposure across T = 10, 50, 100, and 500 years as follows:

Design hydrographs from HEC-HMS were fed as inflows to the 2D domain, enabling the consistent comparison of depth, velocity, and planimetric extent across return periods. For clarity, we report areal extent together with depth/velocity maps, as risk can escalate via severity even when areal growth saturates.

In the analysis of the river's hydraulic modeling for different return periods, a direct relationship was observed between the increase in flow (a product of velocity and depth)

and the expansion of the flooded area, as well as the level of threat to the population, as shown in Figure 11. For a 10-year return period, the estimated flow was 17.13 m^3/s, affecting an area of 7.29 ha, with a predominance of low threat (63.52%), but with 5.33% of the population exposed to very high risk. In the 50-year scenario, the flow increased to 64.75 m^3/s, doubling the affected area to 13.84 ha and raising the proportion of the population at high and very high threat levels to 20.95%, demonstrating a significant increase in risk, even in urban areas adjacent to the riverbed.

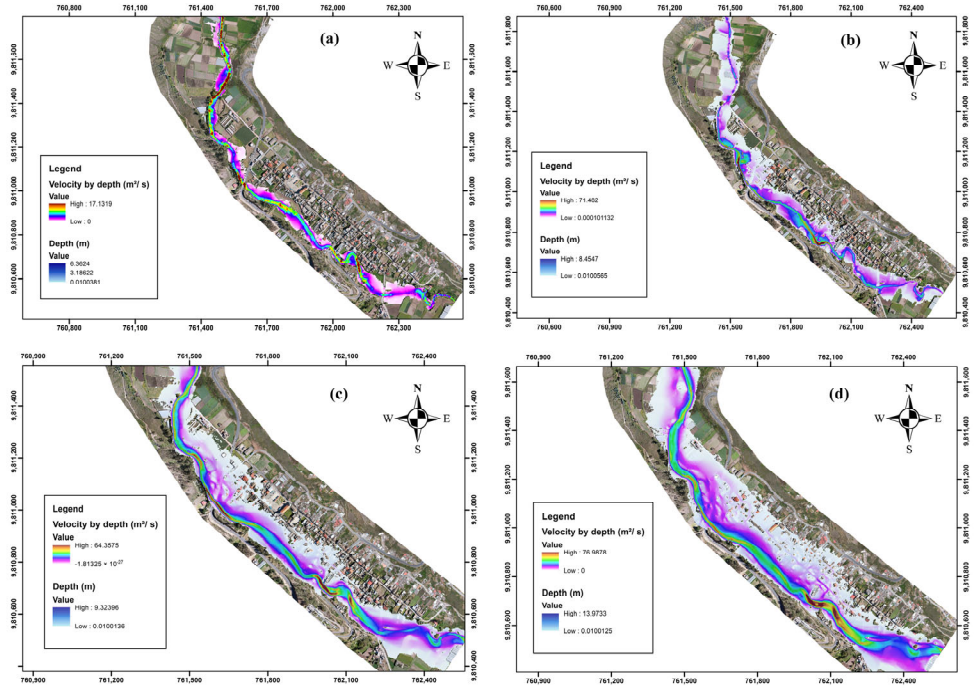


Figure 11. Velocity by depth map for TR of 10 (**a**), 50 (**b**), 100 (**c**), and 500 years (**d**).

For more extreme return periods, the results show increasing impacts in terms of population exposure and infrastructure. In the 100-year scenario, the flow reached 71.48 m^3/s and affected 17.92 ha, with 18.75% of the population at high or very high threat levels. This scenario seriously compromises rural sectors and basic service structures. In the most critical case, with a 500-year period, the estimated flow was 76.98 m^3/s, affecting the same area but with serious consequences for road infrastructure and territorial connectivity. The combination of high flow magnitude and the extent of the flooded area represents a critical challenge for risk management, requiring robust mitigation and response plans.

3.5. Identification and Analysis of Elements Exposed to Flooding in Different Return Periods: 10, 50, 100, and 500 Years

3.5.1. Exposure of Drinking Water and Sewage to Flooding for a Return Period of 10, 50, 100, and 500 Years

As summarized in Table 2, the drinking water system shows low vulnerability to flooding, remaining largely unaffected even in extreme scenarios, although its exposure progressively increases with increasing return periods. In contrast, the sewage system shows an increasing vulnerability trend, reaching critical levels in the 500-year scenario, where almost 75% of its infrastructure is exposed, especially at high and very high levels. This behavior highlights an urgent need for intervention in the sewage system, in contrast to the greater resilience of the drinking water system. Figure 12 illustrates the simulation of the exposure of drinking water and sewage to flooding for return periods of 10, 50, 100, and 500 years.

Table 2. Summary of exposure of drinking water and sewage to flooding.

Return Period	System	Low (%)	Medium (%)	High and Very High (%)	No Impact (%)
10 years	Drinking Water	0.52	0.00	0.00	99.48
	Sewerage	32.30	6.09	8.04	53.57
50 years	Drinking Water	11.44	1.08	0.04	87.44
	Sewerage	28.83	24.60	16.78	29.79
100 years	Drinking Water	23.37	1.74	0.04	74.84
	Sewerage	12.66	24.31	28.57	34.46
500 years	Drinking Water	52.21	4.83	0.08	42.88
	Sewerage	25.04	24.00	49.15	25.81

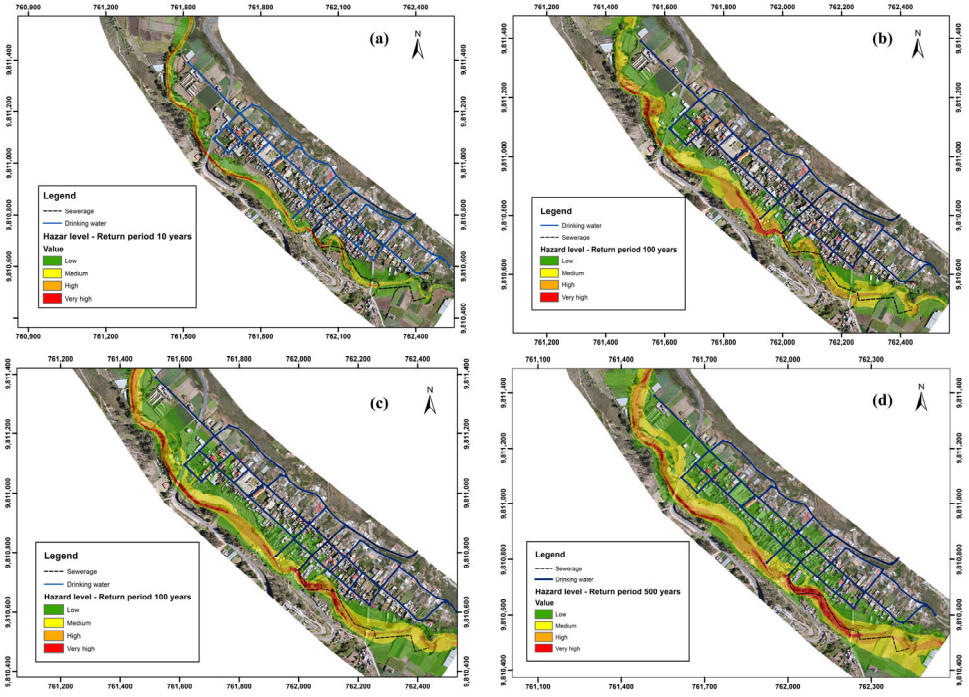


Figure 12. Simulation of the exposure of drinking water and sewage to flooding for a return period of 10 (**a**), 50 (**b**), 100 (**c**), and 500 years (**d**).

3.5.2. Electrical System Exposure to Flooding for a Return Period of 10, 50, 100, and 500 Years

As shown in Figure 13, the high- and low-voltage electrical system shows low vulnerability to flooding in short-term scenarios, especially for a 10-year return period, with more than 90% of the infrastructure remaining undamaged. However, as the return period increases, exposure increases significantly, especially in the 500-year scenario, where less than 40% of the high-voltage infrastructure and less than 45% of the low-voltage infrastructure remain undamaged. Electric poles also reflect this trend, going from minimal impact in mild scenarios to significant vulnerability, with 52.07% exposed in the most extreme scenario. This behavior highlights the need to strengthen the electrical infrastructure to mitigate future risks from extreme hydrometeorological events, as observed in Table 3.

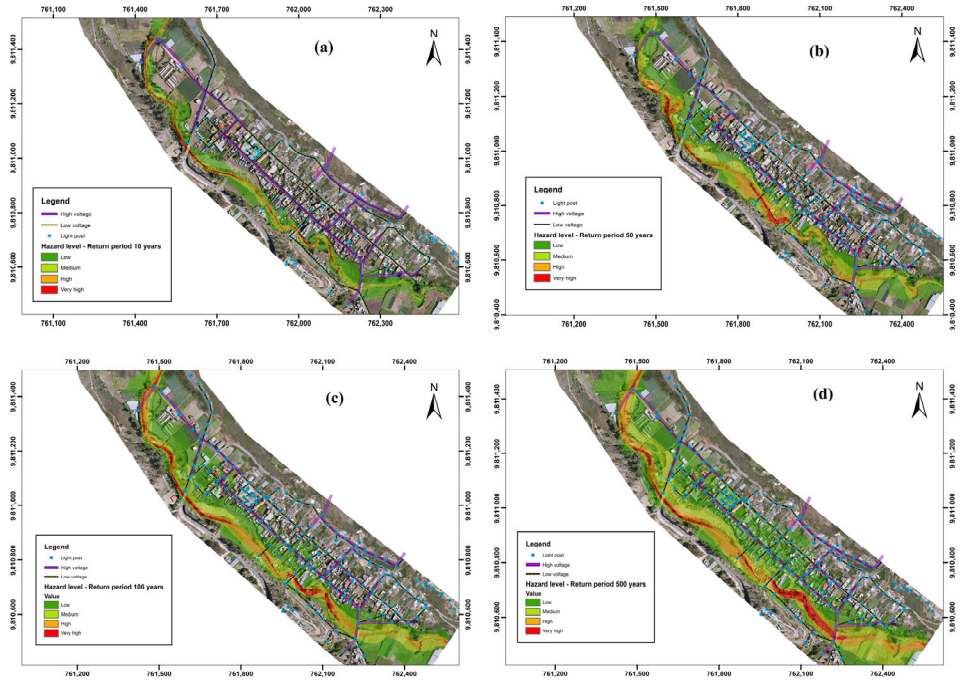


Figure 13. Simulation of the exposure of the electrical system to flooding for a return period of 10 (**a**), 50 (**b**), 100 (**c**), and 500 years (**d**).

Table 3. Summary of electrical system exposure to flooding.

Return Period	System	Low (%)	Medium (%)	High and Very High (%)	No Impact (%)
10 years	High Voltage	6.69	0.60	0.60	92.11
	Low Voltage	1.50	0.60	0.00	97.90
	Electric Poles	0.30	0.29	0.00	98.82
50 years	High Voltage	15.54	2.00	1.82	80.64
	Low Voltage	12.95	1.54	0.00	85.51
	Electric Poles	10.65	1.78	0.00	87.57
100 years	High Voltage	22.00	4.00	5.84	68.16
	Low Voltage	22.46	3.02	0.00	74.52
	Electric Poles	14.79	2.96	0.59	81.66
500 years	High Voltage	48.84	6.00	6.88	38.27
	Low Voltage	34.47	3.65	18.03	43.85
	Electric Poles	42.01	8.88	1.18	47.93

3.6. Direct Economic Damage

Damage estimation using the DaLA adaptation methodology was carried out taking into account the worst-case scenario, which is a return time of 500 years and for the following infrastructure: drinking water and sewage networks, low- and high-voltage power lines, and electric poles. The unit costs for the restoration of infrastructure are presented below: Table 4 for potable-water networks, Table 5 for sewerage networks, Table 6 for electric poles, Table 7 for low-voltage lines, and Table 8 for high-voltage lines.

Table 4. Estimated unit costs for potable water networks.

Component	Estimated Unit Cost (USD/m)
PVC pipe PN10 Ø63–90 mm	17
Excavation for installation (1.0–1.2 m)	10
Valves, tees, fittings (proportional/m)	15
Backfill, compaction, surface restoration	12
Transport and installation	11
Labor	20
Total cost	85

Table 5. Estimated unit costs of sewerage networks.

Component	Estimated Unit Cost (USD/m)
PVC sanitary pipe Ø160 mm SDR41	20
Trench excavation (1.5 m depth)	12
Backfill, compaction, surface restoration	15
Manholes (proportional/m)	18
Transport and handling	10
Labor	25
Total cost	100

Table 6. Estimated unit costs for electric poles.

Component	Estimated Unit Cost (USD/unit)
Concrete pole (12 m)	330
Fittings, insulators, brackets	120
Pole base excavation and foundation	90
Mounting labor	110
Transport and handling	50
Total cost	700

Table 7. Estimated unit costs of low-voltage lines.

Component	Estimated Unit Cost (USD/m)
AAC aluminum cable (3 × 50 mm^2)	6
Insulators and brackets (proportional/m)	3
Connection and protection accessories	1.5
Labor and installation (proportional)	6
Transport and mounting	2.5
Total cost	19

Table 8. Estimated unit costs of high-voltage lines.

Component	Estimated Unit Cost (USD/m)
ACSR aluminum–steel-reinforced cable	8
Polymeric or porcelain insulators	4.5
Fittings and support structures (proportional)	7
Skilled labor	12
Supervision, safety, transportation	6.5
Total cost	38

It is important to indicate that, for the total damage estimate, only the infrastructure segments classified with "high" and "very high" threat levels according to the maps generated in the hydraulic modeling were considered. The results are shown in Table 9.

Table 9. Summary of estimated direct damages.

Infrastructure	Total, Length/Quantity	Unit	High and Very High Damage Level (%)	Unit Cost (USD)	Affected Quantity	Estimated Damage (USD)
Low-Voltage Line	5130.02	m	18.03	22	924.94	20,348.74
High-Voltage Line	2952.46	m	6.88	38	203.13	7718.91
Electric Poles	169	units	1.18	700	1.99	1395.94
Sanitary Sewer Network	1103.16	m	49.15	100	542.2	54,220.31
Water Supply Network	7043.53	m	0.08	85	5.63	478.96
Total Estimated Damage						84,162.86

3.7. Proposals to Reduce the Risk of Flooding

Based on the areas identified with hazard levels, and considering the greater depths and velocities for return times greater than 100 years, the results indicate three lines of action with a direct impact on flood peaks and footprints, which are detailed below:

(i) Protective margins that include exclusion zones and vegetated riparian strips: Their implementation protects the river's buffer zone, reduces bank erosion, and maintains storage capacity in the plain. There is evidence that riparian buffers and vegetation

restoration mitigate the hydrological response, representing a cost-effective measure in urban and peri-urban contexts [33].

(ii) Reinforcement of critical infrastructure: Based on a worst-case scenario with a 500-year return time, these areas, categorized as very high-threat, should consider the selective oversizing of collectors and backflow preventers, the elevation or shielding of electrical equipment above the elevation mark, and the improvement in bridge and culvert crossings using risk-based design criteria [34].

(iii) Telemetry sensors for early warning and adaptive operation: The installation of level-rainfall nodes in control sections of the Chibunga River makes it possible to anticipate overloads and activate protocols that allow for the evacuation of people in the event of river flooding, safeguarding their safety [35].

4. Discussion

4.1. Impact of Flooding on Infrastructure Vulnerability

The study's results on the vulnerability of infrastructures located along the banks of the Chibunga River to flood hazards indicate that the drinking water system exhibits low vulnerability [36]. By contrast, the sewerage system reaches critical levels in the simulation for the 500-year return period, owing to gravity-driven flow and a limited surcharge capacity exacerbated by excessive stormwater inflow, solid intrusion, and potential blockages. Consequently, investments should be prioritized to increase the hydraulic capacity of the sewerage network, whereas only minor adjustments are required for the drinking water system. Regarding the electrical system, flood exposure follows a nonlinear scaling pattern of both exposure and impact severity as return periods lengthen: the proportion of affected assets does not rise proportionally with the hazard but remains relatively stable until physical and capacity thresholds are exceeded. Considering these aspects, it is essential to quantify economic losses under the worst plausible scenario, which was accomplished using the DaLA methodology. This tool is fundamental for demonstrating that preventive action entails lower economic costs than post-disaster reconstruction, thereby fostering a preventive culture and enhancing resilience at the community level. The identification of vulnerable sections of sewage, drinking water, and electrical networks, along with damage estimates based on real unit values (per meter or unit affected), clearly reveals the most critical sectors and guides the prioritization of preventive investments over post-disaster reconstruction. Furthermore, the evidence generated supports the development of public policies that recognize that investment in prevention is not only technically necessary but also economically viable.

4.2. Comparison with Existing Literature

The results show a pattern of hydraulic overload in the sewer system that scales with the return period, consistent with the findings of Aziz et al. [37], who have documented increases in the affected network from 13.31% (Tr = 2) to 26.4% (Tr = 100) due to capacity overruns and excessive rainfall. This study expands that framework by including Tr = 500 years, showing that, in San Luis, the intensification of the hazard is modulated by local construction conditions, such as slopes, incorrect connections of storm drains to the sewer system, obstructions, and expected increases in precipitation. This broader temporal scope allows for the capture of nonlinear damage thresholds (breakpoints) in which small increases in depth/velocity trigger discrete changes in the proportion of compromised assets, a feature that the literature often hints at but rarely quantifies in rural Andean settings.

Unlike studies that focus solely on drinking water/sewerage, this study also incorporates the electrical grid and utility poles, in line with Asaridis et al. [38], in considering

direct damage caused by water–equipment contact, indirect damage caused by losses such as downstream service outages, and systemic damage such as cascading effects on economic activities. Unlike purely hydraulic approaches, the simulation is coupled with exposure mapping and an economic estimate DaLA, in line with Sauer et al. [39] and Mohammadi et al. [40], who emphasize that, in countries with low relative lethality but high mobility/displacement, economic metrics are key to pre-disaster planning. Methodologically, the combined use of ALOS DEM for basin coverage and UAV DEM in critical areas improves the representation of depth–velocity–extent, strengthening the validity of exposure and loss maps, as suggested by [41,42] for small basins with budget constraints.

4.3. Future Research and Limitations

The main limitation of this study lies in the availability and resolution of hydrometeorological data. The characterization was based on satellite products and extrapolated IDF curves, which, although adequate for preliminary estimates, introduces uncertainties due to the low density of stations and the absence of continuous records in the parish of San Luis, a situation that is common in high Andean basins [13,39]. Likewise, the hypothesis of stationarity in precipitation could underestimate future risks associated with climate change.

In topographical terms, the use of ALOS DEM allowed for the low-cost delimitation of the basin, but its resolution limits the detail of microtopography critical for flow propagation. The incorporation of UAV data improved representation in key areas, although without achieving the accuracy of LiDAR DEM reported in studies such as Asaridis et al. [38]. From a modeling perspective, the absence of calibration data—i.e., flood marks, post-event traces, etc.—prevented statistical validation of the hydraulic model, a situation also reported by Aziz et al. [37] in rural environments. Damage assessment focused on direct losses, without considering indirect or systemic impacts, which could underestimate the total risk [34].

Finally, although the DaLA methodology facilitated the estimation of economic losses, unit costs were not exhaustively documented, nor were sensitivity analyses applied, limiting the comparability of results, as suggested by Sauer et al. [38]. Thus, this work stands out for integrating the multiscale vulnerability of drinking water, sewage, and electricity systems in a rural Andean environment, incorporating a 500-year return scenario, which allows for the identification of nonlinear damage thresholds that are not usually evaluated in other studies [37,38]. However, the scarcity of local data, topographical limitations, and the absence of a probabilistic framework for propagating uncertainties represent challenges that, if addressed, strengthen the validity and transferability of the results to other basins with similar characteristics.

5. Conclusions

In this study, an integrated methodology of two-dimensional hydrometeorological and hydraulic analysis was implemented, combining HEC-HMS and the Iber software, in the parish of San Luis (Riobamba, Ecuador) for the following return periods: 10, 50, 100, and 500 years. Based on the hydrodynamic results, depth and velocity values were obtained, as well as risk levels. In addition, the exposure of drinking water networks, sewerage systems, low- and high-voltage electrical systems, and street lighting poles was quantified. On the other hand, direct economic losses were estimated using an adapted version of the DaLA approach. A comparative analysis between scenarios was also carried out to identify critical sections and intervention priorities. The most relevant conclusions are presented below:

- The flooded area increases from 7.29 to 17.92 hectares and the maximum flow increases from 104.6 to 1728.9 m^3/s over the analyzed return periods of 10, 50, 100, and 500 years, demonstrating a nonlinear runoff–conveyance response. This behavior underscores the importance of considering design scenarios with long return periods to ensure resilient infrastructure and appropriate territorial planning.
- The drinking water network is highly resilient, with only 0.08% of its length classified as high-to-very high risk under a 500-year scenario. This implies limited operational loss at modeled extremes. In contrast, 49.15% of the sewer network's pipe length is classified as high-to-very high risk under the worst-case scenario, particularly in low-lying areas. This asymmetry underscores the importance of sewer hydraulics, such as overload control and backflow prevention, as well as right-of-way management, in peripheral sectors. These measures are crucial for mitigating overflows, infiltration, and wastewater diversion during peak demand.
- For high-voltage lines, the proportion of assets in the high-very high class increases from 0.60% in a 10-year scenario to 6.88% in a 500-year scenario. For low-voltage lines, it rises from 0.00% to 18.03%, and for streetlights, it increases from 0.00% to 1.18%. These increases in likelihood, incidence of faults, and access constraints for restoration underscore the importance of span-level hardening, sectionalizing, and elevating or shielding flood-prone equipment.
- The adapted DaLA screening estimates USD 84,162.86 in direct losses under a 500-year scenario. Sewer repairs account for most of these losses, at USD 54,220.31 (64%), followed by low-voltage components, at USD 20,348.74, and drinking water, at USD 479. These figures validate exposure patterns and provide order-of-magnitude inputs for cost–benefit analyses and investment roadmaps.
- Based on these findings, a combined package consisting of the following is imperative: (1) riparian buffers and protective margins to preserve active storage in floodplains and reduce peak flows, (2) targeted reinforcement of sewer choke points and critical electrical components to meet performance targets under a 500-year scenario, and (3) telemetry and an early warning system for adaptive operation. These measures will reduce flood depth and velocity, limit cascading service disruptions, and will provide reproducible information for land use monitoring and sector prioritization.

Author Contributions: Conceptualization, R.M.T. and P.B.-E.; methodology, E.F.R.; software, D.S.P.; validation, D.S.P. and E.F.R.; formal analysis, R.M.T.; investigation, D.S.P.; resources, P.B.-E.; data curation, D.S.P.; writing—original draft preparation, E.F.R.; writing—review and editing, E.F.R. and R.M.T.; visualization, D.S.P.; supervision, E.F.R. and R.M.T.; project administration, P.B.-E.; funding acquisition, R.M.T. and P.B.-E. All authors have read and agreed to the published version of the manuscript.

Funding: This research received no external funding.

Institutional Review Board Statement: Not applicable.

Informed Consent Statement: Not applicable.

Data Availability Statement: The raw data supporting the conclusions of this article will be made available by the authors on request.

Conflicts of Interest: The authors declare no conflict of interest.

References

1. Hirabayashi, Y.; Alifu, H.; Yamazaki, D.; Imada, Y.; Shiogama, H.; Kimura, Y. Anthropogenic Climate Change Has Changed Frequency of Past Flood during 2010–2013. *Prog. Earth Planet. Sci.* **2021**, *8*, 36. [CrossRef]
2. United Nations Office for Disaster Risk Reduction. *La Agenda 2030 y Los Objetivos De Desarrollo Sostenible Una Oportunidad Para América Latina y Caribe*; United Nations Office for Disaster Risk Reduction: Santiago, Chile, 2018; ISBN 978-92-1-058643-6.
3. Nguyen, T.T.; Grote, U.; Neubacher, F.; Rahut, D.B.; Do, M.H.; Paudel, G.P. Security Risks from Climate Change and Environmental Degradation: Implications for Sustainable Land Use Transformation in the Global South. *Curr. Opin. Environ. Sustain.* **2023**, *63*, 101322. [CrossRef]
4. Camacho, A.P.; Ilijama, M.V.; Aroca, G.B.; Betancourt, E.G. Perception of social vulnerability to the climate variability of the population of the microbasin of the Chazo Juan river, Ecuador. *Rev. Geogr. Venez.* **2021**, *62*, 146–159.
5. Torremorell, A.; Hegoburu, C.; Brandimarte, A.; Costa Rodrigues, E.; Pompêo, M.; Silva, S.; Moschini-Carlos, V.; Caputo, L.; Fierro, P.; Mojica, J.; et al. Current and Future Threats for Ecological Quality Management of South American Freshwater Ecosystems. *Inland Waters* **2021**, *11*, 125–140. [CrossRef]
6. Duque, L.-F.; O'Donnell, G.; Cordero, J.; Jaramillo, J.; O'Connell, E. Analysis of the Potential Impacts of Climate Change on the Mean Annual Water Balance and Precipitation Deficits for a Catchment in Southern Ecuador. *Hydrology* **2025**, *12*, 177. [CrossRef]
7. Pinos, J.; Timbe, L. Mountain Riverine Floods in Ecuador: Issues, Challenges, and Opportunities. *Front. Water* **2020**, *2*, 545880. [CrossRef]
8. Güneralp, B.; Güneralp, İ.; Liu, Y. Changing Global Patterns of Urban Exposure to Flood and Drought Hazards. *Glob. Environ. Change* **2015**, *31*, 217–225. [CrossRef]
9. Muis, S.; Verlaan, M.; Winsemius, H.C.; Aerts, J.C.J.H.; Ward, P.J. A Global Reanalysis of Storm Surges and Extreme Sea Levels. *Nat. Commun.* **2016**, *7*, 11969. [CrossRef]
10. Pinos, J.; Quesada-Román, A. Flood Risk-Related Research Trends in Latin America and the Caribbean. *Water* **2022**, *14*, 10. [CrossRef]
11. Wei, Y.; Li, H.; Zhou, Y.; Commey, N.A.; Zhu, Z.; Ishidaira, H.; Jiang, Z.; Yang, D. Flood Vulnerability Assessment of Urban Agglomeration under the Background of Urban Expansion. *J. Hydrol.* **2025**, *662*, 133962. [CrossRef]
12. Bush, S.T.; Dresback, K.M.; Szpilka, C.M.; Kolar, R.L. Use of 1D Unsteady HEC-RAS in a Coupled System for Compound Flood Modeling: North Carolina Case Study. *J. Mar. Sci. Eng.* **2022**, *10*, 306. [CrossRef]
13. Ccanccapa-Puma, J.; Hidalgo-Valdivia, A.V.; Noriega-Aquise, G.Y.; Aguilar-Chávez, A.E.; Marques, M. Analysis and Risk Prevention of Flooding in High-Risk Gorges in the City of Arequipa, Peru. *Tecnol. Cienc. Agua* **2024**, *15*, 6. [CrossRef]
14. Galarza-Villamar, J.A.; Leeuwis, C.; Cecchi, F. Rice Farmers and Floods in Ecuador: The Strategic Role of Social Capital in Disaster Risk Reduction and Livelihood Resilience. *Int. J. Disaster Risk Reduct.* **2024**, *104*, 104332. [CrossRef]
15. Van Niekerk, D.; Nemakonde, L.D.; Kruger, L.; Forbes-Genade, K. Community-Based Disaster Risk Management. In *Handbook of Disaster Research*; Rodríguez, H., Donner, W., Trainor, J.E., Eds.; Springer International Publishing: Cham, Switzerland, 2018; pp. 411–429. ISBN 978-3-319-63254-4.
16. Iglesias-Pascual, R.; Benassi, F.; Ojeda Casares, S.; García, M.Á.H. Social Infrastructure in Southern Europe: A Diagnostic Tool for Socio-Territorial Vulnerability in Public Policies. *Sustain. Dev.* **2025**, *33*, 1–13. [CrossRef]
17. AL-Hussein, A.A.M.; Khan, S.; Ncibi, K.; Hamdi, N.; Hamed, Y. Flood Analysis Using HEC-RAS and HEC-HMS: A Case Study of Khazir River (Middle East—Northern Iraq). *Water* **2022**, *14*, 3779. [CrossRef]
18. Gobierno Autónomo Descentralizado Municipal del Cantón Riobamba. Plan de Ordenamiento Territorial 2023–2035. Available online: https://www.gadmriobamba.gob.ec/index.php/la-municipalidad/la-alcaldia/plan-de-desarrollo-y-ordenamiento/pdot-2023-2035. (accessed on 15 June 2025).
19. United Nations Office for Disaster Risk Reduction. *GAR Special Report 2023: Mapping Resilience for the Sustainable Development Goals*; United Nations Office for Disaster Risk Reduction: Geneva, Switzerland, 2023; ISBN 978-92-1-002830-1.
20. Pérez-Montiel, J.I.; Cardenas-Mercado, L.; Nardini, A.G.C. Flood Modeling in a Coastal Town in Northern Colombia: Comparing MODCEL vs. IBER. *Water* **2022**, *14*, 3866. [CrossRef]
21. Rivera Guzmán, E.F.; Mañay Chochos, E.D.; Chiliquinga Malliquinga, M.D.; Baldeón Egas, P.F.; Toasa Guachi, R.M. LoRa Network-Based System for Monitoring the Agricultural Sector in Andean Areas: Case Study Ecuador. *Sensors* **2022**, *22*, 6743. [CrossRef]
22. Earth Science Data Systems Phased Array L-Band Synthetic Aperture Radar. Available online: https://www.earthdata.nasa.gov/data/instruments/palsar (accessed on 24 July 2025).
23. Valdivia Pompa, H.A.; Cerdan Mendoza, J. *Niveles de Precisión en Medición de Caudales Utilizando el Método Del Flotador*; Universidad Privada del Norte: Cajamarca, Perú, 2023.
24. SERCOP Búsqueda de Procesos de Contratación. Available online: https://www.compraspublicas.gob.ec/ProcesoContratacion/compras/PC/buscarProceso.cpe?sg=1 (accessed on 5 August 2025).

25. Ávila Parra, K.; Martín Vide, J. Análisis estadístico de los eventos extremos de precipitación en la zona centro y sur de Chile continental. *Cuad. Geográficos* **2013**, *52*, 69–83. Available online: https://revistaseug.ugr.es/index.php/cuadgeo/article/view/926 (accessed on 5 August 2025).
26. Tenesaca-Saca, M.E.; Reyes-Zambrano, J.L.; Vallejo-Vizhuete, D.P.; Chavarría-Párraga, J.E. Modelación Hidrológica e Hidráulica para la Identificación de Zonas de Inundación en la Quebrada Las Abras, Riobamba. *Rev. Cient. INGENIAR Ing. Tecnol. Investig.* **2024**, *7*, 323–343. Available online: https://journalingeniar.org/index.php/ingeniar/article/view/228 (accessed on 5 August 2025).
27. Chow, V.T.; Maidment, D.R.; Mays, L.W. *Applied Hydrology*; McGraw-Hill: New York, NY, USA, 1988; ISBN 0-07-010810-2.
28. Zolghadr, M.; Rafiee, M.R.; Esmaeilmanesh, F.; Fathi, A.; Tripathi, R.P.; Rathnayake, U.; Gunakala, S.R.; Azamathulla, H.M. Computation of Time of Concentration Based on Two-Dimensional Hydraulic Simulation. *Water* **2022**, *14*, 3155. [CrossRef]
29. Snyder, F.F. Synthetic Unit Graphs. *Trans. Am. Geophys. Union* **1938**, *19*, 447–454. [CrossRef]
30. Chow, V.T. *Open-Channel Hydraulics*; The Blackburn Press: Caldwell, NJ, USA, 2009; ISBN 978-1-932846-18-8.
31. Barnes, H. *Roughness Characteristics of Natural Channels*; USGS: Reston, VA, USA, 1967.
32. Arcement, G.; Schneider, V. *Guide for Selecting Manning's Roughness Coefficients for Natural Channels and Flood Plains*; USGS: Reston, VA, USA, 1989.
33. Valera, C.A.; Pissarra, T.C.T.; Filho, M.V.M.; Do Valle Júnior, R.F.; Oliveira, C.F.; Moura, J.P.; Sanches Fernandes, L.F.; Pacheco, F.A.L. The Buffer Capacity of Riparian Vegetation to Control Water Quality in Anthropogenic Catchments from a Legally Protected Area: A Critical View over the Brazilian New Forest Code. *Water* **2019**, *11*, 549. [CrossRef]
34. Avcı, C.B.; Vanolya, M. Proposed Framework for Sustainable Flood Risk-Based Design, Construction and Rehabilitation of Culverts and Bridges Under Climate Change. *Water* **2025**, *17*, 1663. [CrossRef]
35. Esposito, M.; Palma, L.; Belli, A.; Sabbatini, L.; Pierleoni, P. Recent Advances in Internet of Things Solutions for Early Warning Systems: A Review. *Sensors* **2022**, *22*, 2124. [CrossRef]
36. Fekete, A.; Estrany, J.; Ramírez, M.Á.A. Cascading Impact Chains and Recovery Challenges of the 2024 Valencia Catastrophic Floods. *Discov. Sustain.* **2025**, *6*, 586. [CrossRef]
37. Aziz, F.; Wang, X.; Qasim Mahmood, M.; Guild, R. Wastewater Flooding Risk Assessment for Coastal Communities: Compound Impacts of Climate Change and Population Growth. *J. Hydrol.* **2024**, *645*, 132136. [CrossRef]
38. Asaridis, P.; Molinari, D.; Di Maio, F.; Ballio, F.; Zio, E. A Probabilistic Modeling and Simulation Framework for Power Grid Flood Risk Assessment. *Int. J. Disaster Risk Reduct.* **2025**, *120*, 105353. [CrossRef]
39. Sauer, I.J.; Mester, B.; Frieler, K.; Zimmermann, S.; Schewe, J.; Otto, C. Limited Progress in Global Reduction of Vulnerability to Flood Impacts over the Past Two Decades. *Commun. Earth Environ.* **2024**, *5*, 239. [CrossRef]
40. Mohammadi, S.; De Angeli, S.; Boni, G.; Pirlone, F.; Cattari, S. Review Article: Current Approaches and Critical Issues in Multi-Risk Recovery Planning of Urban Areas Exposed to Natural Hazards. *Nat. Hazards Earth Syst. Sci.* **2024**, *24*, 79–107. [CrossRef]
41. Bashir, B.; Alsalman, A. Morphometric Characterization and Dual Analysis for Flash Flood Hazard Assessment of Wadi Al-Lith Watershed, Saudi Arabia. *Water* **2024**, *16*, 3333. [CrossRef]
42. Annis, A.; Nardi, F.; Petroselli, A.; Apollonio, C.; Arcangeletti, E.; Tauro, F.; Belli, C.; Bianconi, R.; Grimaldi, S. UAV-DEMs for Small-Scale Flood Hazard Mapping. *Water* **2020**, *12*, 1717. [CrossRef]

Disclaimer/Publisher's Note: The statements, opinions and data contained in all publications are solely those of the individual author(s) and contributor(s) and not of MDPI and/or the editor(s). MDPI and/or the editor(s) disclaim responsibility for any injury to people or property resulting from any ideas, methods, instructions or products referred to in the content.